mater.scichina.com link.springer.com

Published online 6 May 2023 | https://doi.org/10.1007/s40843-022-2424-4
Sci China Mater 2023, 66(7): 2872–2884

Effects of carbonate species and chloride ions on calcium phosphate nucleation of biological apatite

Hongwei Chen[1†], Junlin Wang[2†], A.E. Willaims-Jones[3], Qin Zhu[1], Lifeng Zheng[1], Chenchen Zhao[1], Ziteng Liu[1], Weigao Xu[1], Haizhen Wei[2*], Lin Guo[1*] and Jing Ma[1*]

ABSTRACT **Apatite is the principal inorganic component of biological hard tissues such as bone and teeth, and thus is essential to the existence of vertebrate life. Because carbonate species and chloride ions are ubiquitous in the fluids of vertebrate life forms, and these species are known to compete with phosphate species, it is critical to understand the influence of these anions on the nucleation of biological apatite. In this study, the important roles of carbonate and chloride ions in mediating inorganic calcium phosphate (CaP) phase nucleation are revealed both theoretically and experimentally. Theoretical investigations suggest that the Ca–O coordination number is an important descriptor for the nucleation of CaP and the interface interaction of the CaP-additive. Positive surface charges on the outermost Ca^{2+} ions of CaP clusters could attract carbonate species and Cl^- ions, promoting the formation of CaP phase. In the presence of carbonate species and Cl^- ions, the crystallization of hydroxyapatite (HA) from its precursor brushite (DCPD) has been observed in our experimental studies. The Cl^- ion-doped B-type HA is proposed to be the most likely biological apatite based on equilibrium oxygen isotope fractionation and vibrational spectroscopic analysis. The insight gained here may help rationalize the control of biomineralization, and will guide the synthesis of anion-doped biological functional apatite materials.**

Keywords: calcium phosphate, Cl^- ion, carbonate species, coordination number, surface energy, simulated body fluid solution

INTRODUCTION

Living organisms produce hierarchically structured materials with unique structures and functions such as bone/teeth and shells, which consist of calcium phosphate (CaP) and $CaCO_3$ (calcite, aragonite, and vaterite) [1]. CaP is the principal inorganic constituent (~60 wt%) of bone, and the main constituent (90%) of tooth enamel [2]. Hydroxyapatite (HA, $Ca_{10}(PO_4)_6(OH)_2$) is the most thermodynamically stable phase in CaP minerals with good biocompatibility, bioactivity, osteoinduction, and nontoxicity [3–5]. Biological apatites, which are usually calcium-deficient and carbonate-substituted, are the minerals of calcified tissues (dentin and bone) and differ slightly from pure HA in stoichiometry, chemical composition and crystallinity [6,7], as shown in Table 1.

The formation of biological apatite generally requires the regulation of enzymes, such as carbonic anhydrase (CA) and alkaline phosphatase (ALP) [8], at ambient temperature and pressure. Nucleation of various CaP morphologies as well as the phase transformation from calcium-deficient brushite (DCPD, Ca/P = 1.00) to HA (Ca/P = 1.67) can be manipulated by a variety of factors including temperature [9,10], initial pH value [11], inorganic cations (Ca^{2+} and Mg^{2+}) [12,13], and the addition of organic species such as dopamine (DA) [14], cellulose (GLU_n) [15], acetic acid (HAc) [16], lactic acid (LAC) [17], acidic amino acids (Asp, Glu), [18] and citrate [19] (Table 1). In addition, the anions of carbonate species and Cl^- ions are ubiquitous in both body fluids of biological systems and a variety of geological settings, but it still remains unknown how these anions stabilize the CaP phase and regulate CaP phase in ambient condition.

In contrast to biological apatite, geological apatite is a versatile mineral with a general formula of $A_5(XO_4)_3Z$ (Table 1) which incorporates a diverse range of major and trace elements, including halogens, and is stable over a wide pressure and temperature (*P-T*) range (up to 12 GPa and 1500°C) [20]. Apatite is widely distributed in magmatic, metamorphic, and hydrothermal rocks and is an excellent repository for recording a variety of geological processes. Because of its high sensitivity to fluid activity, apatite has great potential to trace the origin, migration, enrichment, and precipitation mechanism of key elements in ore-forming fluids due to the complicated substitution pathways of ionic species, such as CO_3^{2-}, F^-, Cl^-, OH^-, Na^+, and rare earth element (REE^{3+}) [21,22]. The role of CO_3^{2-} and Cl^- ions in the nucleation process of biological apatite needs to be investigated, which will provide a basis for understanding the formation mechanism of geological and biological apatites.

The mechanisms by which apatite crystallizes are poorly understood for a wide range of *P-T-x-y* conditions (*x* and *y* denote the chemical composition and factors of regulation, respectively). This work attempts to discover the role of carbonate species and Cl^- ions in the early nucleation process of CaP, to understand the growth of its crystals *via* the interfacial interactions of CaP clusters with additives, and to identify the most likely composition of biological apatite in nature. The

[1] Key Laboratory of Mesoscopic Chemistry of Ministry of Education, School of Chemistry and Chemical Engineering, Nanjing University, Nanjing 210023, China
[2] State Key Laboratory for Mineral Deposits Research, Department of Earth Sciences and Engineering, Nanjing University, Nanjing 210023, China
[3] Department of Earth and Planetary Sciences, McGill University, Montreal H3A 0E8, Canada
[†] These authors contributed equally to this work.
[*] Corresponding authors (emails: majing@nju.edu.cn (Ma J); haizhenwei@nju.edu.cn (Wei H); linguo@nju.edu.cn (Guo L))

Table 1 Biological apatite and geological apatite

Features	Details of apatite	Ref.
	Biological apatite (bone, teeth)	
Chemical composition	$Ca_{9.3\pm0.7}(PO_4)_{4.3}(HPO_4, CO_3)_{1.7}(OH, CO_3)_{0.3\pm1.7}$	[23]
Ca/P ratio	≤ 1.67	[7,23]
Interaction with ions	HCO_3^-, Cl^-, F^-, Na^+, K^+, Mg^{2+}, etc.	[24]
Interaction with organic additives	Glutathione (GSH/GSSG), DA, GLU_n, CH_3COOH (HAc), LAC, acidic amino acids (Asp and Glu), citrate, etc.	[14–19]
Interaction with biomolecules	Collagen Non-collagenous proteins (osteocalcin, etc.)	[24,25]
	Geological apatite	
Chemical composition	$A_5(XO_4)_3Z$ A = Ca^{2+}, Sr^{2+}, Mg^{2+}, REE^{3+}, etc. X = P^{5+}, Si^{4+}, S^{6+}, etc. Z = OH^-, Cl^-, F^-	[26–28]
Ca/P ratio	> 1.67	[20,27]
Stability fields	HA is stable under T < 950°C and P <7.5 GPa HA is stable under T < 1300°C and P <12 GPa Fluorapatite is stable under T < 1500°C and P <12 GPa	[29] [30]
Types	Magmatic apatite, hydrothermal apatite, etc.	[31,32]

significant increase in understanding of biomineralization by investigating the role of carbonate species and Cl^- ions in the nucleation of CaP will help in the design of anion-doped biocompatible apatite materials and contribute to the understanding of geological apatite stabilization mechanisms.

COMPUTATIONAL AND EXPERIMENTAL SECTION

Surface energy of B-HA-Cl

The surface stability of B-type Cl^--doped HA ($Ca_{10}(PO_4)_5(CO_3$-$Cl)(OH)_2$, B-HA-Cl) was related to its surface energy (E_{surf}), which was computed with the following equation [33]:

$$E_{surf} = (E_{slab} - nE_{bulk})/2A, \quad (1)$$

where E_{slab} and E_{bulk} are the energies of the n layers of slab and the B-HA-Cl bulk, respectively, and A is the area of the surface unit cell. A small E_{surf} value indicates a relatively stable surface.

The vacuum layer of the slab model was set to 30 Å with a thickness of four layers. The calculations were carried out to optimize the slab structures with the plane-wave expansion limited to a cutoff energy of 550 eV and a self-consistent field (SCF) convergence of 0.04 eV $Å^{-1}$. Brillouin zone sampling for the B-HA-Cl (001) surface was performed using the Monkhost-Pack scheme with a k-point grid of 4 × 4 × 1 (4 × 4 × 5 for bulk).

Binding strength predicted by density functional theory calculations and machine learning

To study the influence of pH values and additives on the interfacial interactions of CaP with the surrounding species, the binding strengths of free Ca^{2+}, CaP, and calcium carbonate (CaC) clusters with additives (Y), were calculated using the density functional theory (DFT) with the polarizable continuum model (PCM) at the level of M062X/6-311+g(d,p). The geometrical optimizations of the studied compounds were performed by using the Gaussian 16 package [34]. The binding free energy (ΔG_b^{DFT}) of a compound at a given pH was determined using the following equations:

$$\Delta G_b^{DFT} = G_{NY} + 6 \times G_{wt} - G_Y - G_{Ca(wt)_6}, \quad (2)$$

$$\Delta G_b^{DFT} = G_{MY} + 6 \times G_{wt} - G_Y - G_X - G_{Ca(wt)_6}, \quad (3)$$

where N = Ca^{2+}, M = CaC and CaP clusters, Y = GSH (Fig. S1), GSSG, LAC, GLU_n, Glu, Asp, HAc, citric acid, and DA, X = $H_2PO_4^-$, HPO_4^{2-}, H_2CO_3, HCO_3^-, and CO_3^{2-}.

The crystal or slab model with the periodic boundary condition was applied to simulate the binding of additives on the DCPD (020), HA (001), and HA (100) surfaces using DFT calculations. The DFT calculations were performed by using the generalized gradient approximation (GGA) with Perdew-Burke-Ernzerhof (PBE) [35] functional as implemented in plane wave-based Vienna *ab initio* simulation package (VASP) [36]. The van de Waals (vdW) correction with the Grimme approach (DFT-D3) [37] was performed to describe the interaction between the additive species and surfaces.

Machine learning (ML) algorithms were performed in the Python3 environment by the open source Scikit-learn [38]. Gradient boosting regression (GBR), extreme gradient boosting (XGBoost), and multiple linear regression (MLR) models were applied to predict the DFT binding energies (E_b^{DFT}) between additives (HAc, LAC, GSH, DA, Glu, Asp, and citric acid) and the DCPD/HA surfaces with different Ca/P ratios. The 178 binding sites were obtained based on the adsorption of additives on DCPD and HA surfaces with different Ca/P ratios [17]. The DFT calculation data were randomly scrambled and divided into a training set and a test set with a ratio of 80:20. All the data were normalized before the modeling. To reduce the risk of overfitting and underfitting, 10-fold cross-validation was applied for model selection. The prediction ability was evaluated by the mean absolute error (MAE) and Pearson's correlation coefficient (r).

$$MAE = \frac{1}{n}\sum_{i=1}^{n}\left|y_i - y_i^{predict}\right|, \quad (4)$$

$$r = \frac{\sum_{i=1}^{n}\left(y_i - y_{\text{mean}}^{\text{test}}\right) \times \left(y_i^{\text{predict}} - y_{\text{mean}}^{\text{predict}}\right)}{\sum_{i=1}^{n}\left(y_i - y_{\text{mean}}^{\text{test}}\right)^2 \times \sum_{i=1}^{n}\left(y_i^{\text{predict}} - y_{\text{mean}}^{\text{predict}}\right)^2}, \quad (5)$$

where y_i, y_i^{predict}, $y_{\text{mean}}^{\text{predict}}$, and $y_{\text{mean}}^{\text{test}}$ are the actual DFT calculation values, ML predicated results, average DFT calculation values, and average ML predicated results, respectively.

Molecular dynamics simulations of aggregation and nucleation

To study the nucleation process of CaP or CaC in the absence and presence of additives (GSH and GSSG), we carried out molecular dynamics (MD) simulations. All MD simulations were carried out with the AMBER16 (CUDA version) [39] simulation package, adopting the general AMBER force field (GAFF2) [40] with the restricted electrostatic potential (RESP) method to fit the charges of the phosphate species, carbonate ions and additives (MP2/6-311+g(d,p)). The GAFF2 force field was used for the phosphate species and carbonate species, with the force field parameters listed in Tables S1 and S2. The 500-ns MD simulations were run at NPT ensemble (with a constant pressure of 1.0 bar and temperatures of 300 and 310 K) for the model systems. The temperature was controlled using Langevin dynamics with the collision frequency of 1 ps^{-1}. The integration step was set as 1 fs. The direct spatial nonbonded cutoff of 8.0 Å was used. The adaptive Poisson-Boltzmann Solver (APBS) [41] was employed to study the electrostatic properties of CaP and CaC clusters. For each simulation model, the MD simulations were repeated three times independently, and the averaged value was obtained by averaging the results of these individual simulations.

Equilibrium oxygen isotope fractionation of phosphate and carbonate minerals

According to the Bigeleisen and Mayer equation or Urey theory [42,43], the equilibrium isotope fractionation due to changes in vibrational frequencies is caused by isotopic substitution in a given system. The reduced isotopic partition function ratio (RPFR) of element X between phase A and a monatomic ideal gas can be calculated by the harmonic approximation:

$$\text{RPFR(X)} = \frac{Z^*}{Z} = \prod_i^N \frac{u_i^*}{u_i} \frac{\exp\left(-\frac{u_i^*}{2}\right)}{1-\exp(-u_i^*)} \frac{1-\exp(-u_i)}{\exp\left(-\frac{u_i}{2}\right)}, \quad (6)$$

where Z^* and Z refer to the vibrational partition function for the heavy and light isotopes, respectively, N is the total number of vibration modes, and the subscript i is the vibration mode order number.

For convenience, the RPFR was converted to the β factor using the relationship of $\beta = \text{RPFR}^{1/n}$. The exponent of $1/n$ is a normalizing factor to account for multiple substitutions in substance A containing more than one atom of X. The term of u_i (u_i^*) was calculated from the relationship:

$$u_i = \frac{hc \times \nu_i}{kT}, \quad (7)$$

where h is the Plank's constant, c is the speed of light, ν_i is the frequency of vibration in cm^{-1}, k is the Boltzmann's constant, and T is the temperature in Kelvin.

The isotope fractionation at equilibrium between phases A and B can be expressed as [44]

$$\Delta_{\text{A-B}} \approx 1000\ln\alpha_{\text{A-B}} = 1000\ln\beta_{\text{A}} - 1000\ln\beta_{\text{B}}. \quad (8)$$

All calculations were carried out using the Cambridge Serial Total Energy Software Package (CASTEP) [45]. The GGA method together with PBE, and norm-conserving pseudopotentials were employed in both geometric optimizations and phonon frequency calculations for the PBC model of the phosphate and carbonate minerals.

Experimental materials and characterization

Calcium chloride ($CaCl_2{\cdot}2H_2O$), diammonium hydrogen phosphate ($(NH_4)_2HPO_4$), sodium hydrogen carbonate ($NaHCO_3$), *L*-glutathione reduced (GSH), and *L*-glutathione oxidized (GSSG) were purchased from Sinopharm Chemical Reagent Co., Ltd. The commercial simulated body fluid (SBF) solution (Table S3) was acquired directly from Shanghai Yuanye Bio-technology Co., Ltd. All chemicals were used without further purification.

X-ray diffraction (XRD) analyses of the crystalline structures of the as-prepared products were conducted on a X'TRA instrument with Cu Kα radiation (λ = 0.154 nm) generated at 40 kV and 40 mA. The morphology and energy-dispersive X-ray spectroscopy (EDS) mapping images of as-prepared samples were characterized using scanning electron microscopy (SEM, S-3400N) operating at 20 kV. The chemical groups of the as-prepared samples were analyzed by infrared (IR) spectra (VERTEX 70, Bruker) for the range from 4000 to 400 cm^{-1}. The CaP precipitation was recorded using a ultraviolet-visible (UV-Vis) spectrophotometer (METTLER TOLEDO) in the spectral range of 190–1000 nm. The compositions of samples were detected by inductively coupled plasma atomic emission spectroscopy (ICP-AES, Perkin Elmer Avio500).

RESULTS AND DISCUSSION

In an attempt to understand the early stage of biomineralization under mild temperature conditions in the presence of the SBF solution and some organic additives, we carried out a sequential multi-scale study of CaP systems, ranging from the electronic structure level through the atomic to molecular level, including equilibrium oxygen isotope fractionation among minerals to the macroscopic morphology properties. The surface energy and interfacial binding energy, which were evaluated by using DFT and ML models, are helpful for understanding the driving force of CaP aggregation at the electronic scale. Atomic-level MD simulations were run to trace the formation of the pre-nucleation clusters at the early stage of the nucleation process. In addition, an atomic-level survey of the equilibrium oxygen isotope fractionation between carbonates and apatite-group minerals, including specific oxygen sites in HA using DFT was compared with experimental observation, linking the electronic structure to the exact chemical compositions of apatite crystals in nature.

Surface stability and early nucleation of CaP systems

The DFT calculated E_{surf} indicates that the HPO_4-exposed (020) surface in DCPD/HA surfaces is the most stable with the largest coordination number of upmost Ca^{2+} on surface, $n_{\text{Ca}}^{\text{Surf}}$ (Fig. 1a and Table S4). This implies that $n_{\text{Ca}}^{\text{Surf}}$ is an important descriptor for rationalizing the relative surface stability of apatite. In addition, the E_{surf} of terrestrial apatite-group minerals can be roughly divided into two categories (Table S5). The fluorapatite

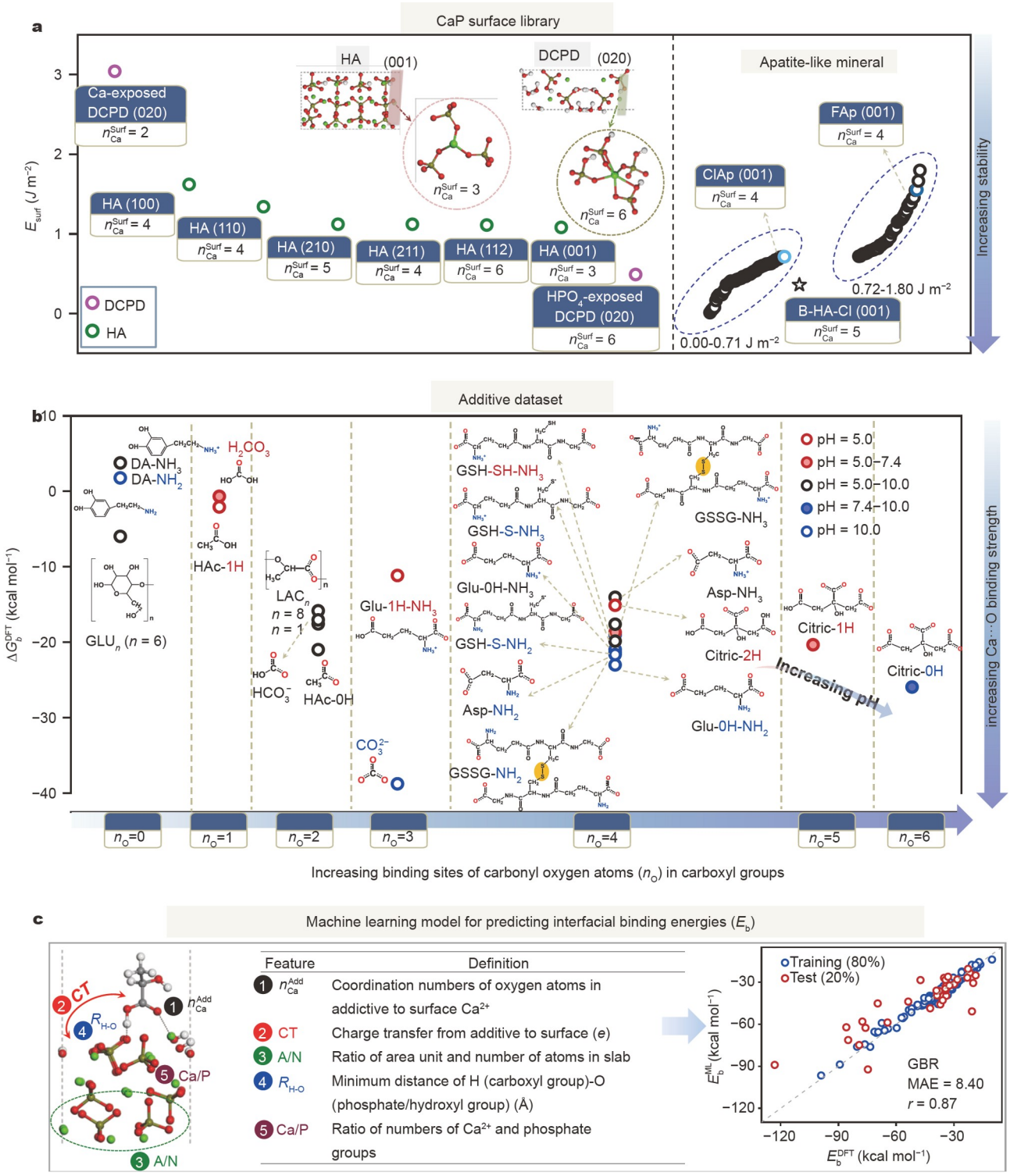

Figure 1 Feature learning of binding energy. (a) The calculated E_{surf} (J m^{-2}), for the selected surfaces of DCPD, HA, and apatite-group minerals. (b) The calculated ΔG_{Ca}^{Tot} (kcal mol^{-1}) between additives and free Ca^{2+} ions as the n_O increases. (c) The definition of selected features and comparison of the E_b predicted from ML with those predicted from DFT.

(FAp) (100) surface is less stable than the chlorapatite (ClAp) (100) surface, suggesting that Cl^- ion doping could make the minerals more stable kinetically. It will be shown in the following subsection that the proposed biological-like apatite, Cl^--doped B-HA-Cl (001) has a lower surface energy (E_{surf} = 0.36 J m^{-2}) than the HA (001) surface (E_{surf} = 1.08 J m^{-2}). The $CaCl_2$ molecule has higher solubility and hence a higher Ca coordination number, 5 in $CaCl_2(H_2O)_6$ *versus* 2 in CaF_2 [46]. Thus, it seems that the stability of the CaP phase could be increased by reacting with a Cl^--bearing solution such as SBF

solution.

In the calculation of surface energy, the slab models consisting of the solid-vacuum surface of CaP were built. As could be seen from Fig. 1a, the surface energies of the CaP systems varied with the crystal surfaces (HA) and surface exposed groups (DCPD). In the DCPD (020) surface, the surface Ca^{2+} coordination number n_{Ca}^{Surf} is 6, while the surface Ca^{2+} coordination number is 3 for HA (001) surface. The surface Ca^{2+} ion with a low coordination number can further bind additives to stabilize this interface and promote the CaP nucleation. The greater the binding free energy of an additive to Ca^{2+} ion, the stronger the binding to the CaP surface. Additives such as Asp and Glu, can decrease the interfacial energy barrier significantly and induce the HAP formation on DCPD [18].

The surface stability of CaP species is also affected by additives. The ΔG_b^{DFT} between additives and free Ca^{2+} ions increased as the number of carboxyl groups (n_O) increased (Fig. 1b and Tables S6–S9). In comparison with GLU_6 and DA, which do not contain carboxyl oxygen ($n_O = 0$), additives such as LAC ($n_O = 2$) have greater ΔG_b^{DFT} (−17.57 kcal mol^{-1}), considering that the number of carboxyl group in the additives enabled us to qualitatively characterize their ability to modulate CaP nucleation. The pH condition affected the protonation states of the additives, e.g., citric acid had two hydrogen atoms at pH of 5.0 (citric-2H), one hydrogen atom at pH of 5.0–7.4 (citric-1H), and no hydrogen atoms at pH of 7.4–10.0 (citric-0H f) in its carboxyl groups. This in turn altered the ΔG_b^{DFT} of citric acid species with Ca^{2+} ions (Fig. 1b). The ΔG_b^{DFT} data of various additives with CaC and CaP clusters had similar pH-dependence (Table S9).

The interfacial binding energy (E_b^{DFT}, Section S1 of the Supplementary Information) is also related to the Ca coordination and hydrogen binding modes between the additive and substrate. For example, HAc and LAC are capable of undergoing multiple interactions with the surface species of HA/DCPD surfaces, leading to a greater binding strength than in the case of single-site binding situation [17]. Feature engineering screened out five well-performed descriptors, n_{Ca}^{Add}, charge transfer (CT), the ratio of the area unit and the number of atoms (A/N), the distance of H–O bond (R_{H-O}), and Ca/P ratio (Fig. 1c). Among them, the descriptors of n_{Ca}^{Add}, CT, and A/N successfully describe the interfacial bindings of additives with CaP surfaces. The strong binding ability of the additive with the surface Ca^{2+} ions was expected to regulate the formation of CaP phase. The occurrence of proton transfer from a carboxyl group of an additive to phosphate group on the surface was depicted by a short interatomic distance (less than 1.2 Å) between H and O, R_{H-O}. The Ca/P ratio was used to evaluate the calcium-deficient state of the CaP system upon the addition of various additives on the CaP surface. After the training from 178 binding energies of different additives on DCPD or HA surfaces with different Ca/P ratios, a good prediction was achieved with GBR, better than the other two ML models, XGBoost and MLR (Fig. 1c and Fig. S2).

MD simulations (Section S2 of the Supplementary Information and Tables S10–S18) were used to investigate the effect of carbonate species and Cl^- ions on the CaP nucleation. The effect of additives on CaP nucleation was also studied. Our emphasis was on the addition of glutathione (γGlu-Cys-Gly), which is one of the most ubiquitous and important small biomolecules in cells of all organisms [47]. Such a tripeptide can be found in reduced thiol (GSH) or oxidized disulfide (GSSG) states (Fig. 1b and Fig. S1). The GSH can also prevent damage to important cellular components caused by reactive oxygen species (ROS), such as free radicals [48]. The MD simulated evolution process of the early cluster aggregation was evaluated with a size descriptor, n_{Ca}^{Tot}, which was the average Ca–O (from all oxygen-containing species) coordination number within the cutoff distance (Figs S3–S6). The distribution of n_{Ca}^{Tot} was in the range of 3–10 (Figs S7–S9) with the most populated n_{Ca}^{Tot} located at 8 and 7, consistent with the Car-Parrinello MD simulation results [49].

The growth of the aggregated CaP cluster was indicated by the largest cluster size [17], n_{size}, in the presence and absence of additives. The oxygen-containing groups of additives can chelate with Ca^{2+} ions of CaP clusters, decreasing the contact opportunity of Ca^{2+} ions with phosphate species, thereby forming the smaller CaP cluster n_{size} with less populated positive charge on particle surface in both neutral and alkaline conditions (Fig. S10).

As the pH increased, the binding strength ΔG_b^{DFT} of the phosphate species with Ca^{2+} ions gradually increased with the increase of the oxygen number, n_O, resulting in the average Ca–O (from phosphate species) coordination number, n_{Ca}^{Pho}, increasing from about 1.0 (pH ≈ 5.0) to about 4.0 (pH ≈ 13.0) in the absence of additives (Fig. 2a, Table S19, and Figs S11 and S12). Under the alkaline conditions, the additives reduced the n_{Ca}^{Pho} value, whereas under acidic conditions n_{Ca}^{Pho} value only changed slightly because of the relatively low binding free energies of the phosphate species/additives with Ca^{2+} ions. In addition, Ca^{2+} ions exposed on the surface of CaP clusters (Fig. S10) attracted negatively charged ions such as Cl^- and HCO_3^- through electrostatic interaction, promoting the formation of a CaP phase in the Cl^-- and CO_3^{2-}-bearing SBF solution. The role of Cl^- and CO_3^{2-} ions in stabilizing the pre-nucleation CaP clusters was further assessed in MD simulations with the carbonated CaP system in SBF solution (Fig. 2b and Fig. S13).

The addition of phosphate did not affect the aggregation of $CaCO_3$ within the given simulation time, as reflected by the n_{Ca}^{Car}, n_{size} of the CaC cluster, and the ratio of Ca/C in carbonate (Fig. 2b and Fig. S14). The presence of additives led to a smaller ratio of Ca/P or Ca/C due to the reduced opportunity for the additive-capped Ca^{2+} ions to further coordinate with phosphate species or CO_3^{2-} ions. Temperature also had a small effect on the n_{Ca}^{Pho} of the HA system without additives (Figs S15 and S16). The CO_3^{2-} ions were able to compete with phosphate in binding with Ca^{2+} ions, resulting in a smaller value of n_{Ca}^{Pho} in the carbonated HA system compared with HA in the absence of additives (Fig. 2b and Fig. S16). The decrease in n_{Ca}^{Pho} is mainly attributed to the loss of water molecules that were coordinated to Ca^{2+} ions and the decrease in the number of free Ca^{2+} and phosphate ions (Figs S17–S20). The decrease in the number of free Ca^{2+} ions and phosphate species is consistent with MD simulation results reported previously [50]. The n_{Ca} is hence a key descriptor in the early nucleation process of CaP.

To further study the aggregation process of CaP, we also constructed two larger-sized CaP systems with 192 free Ca^{2+} ions

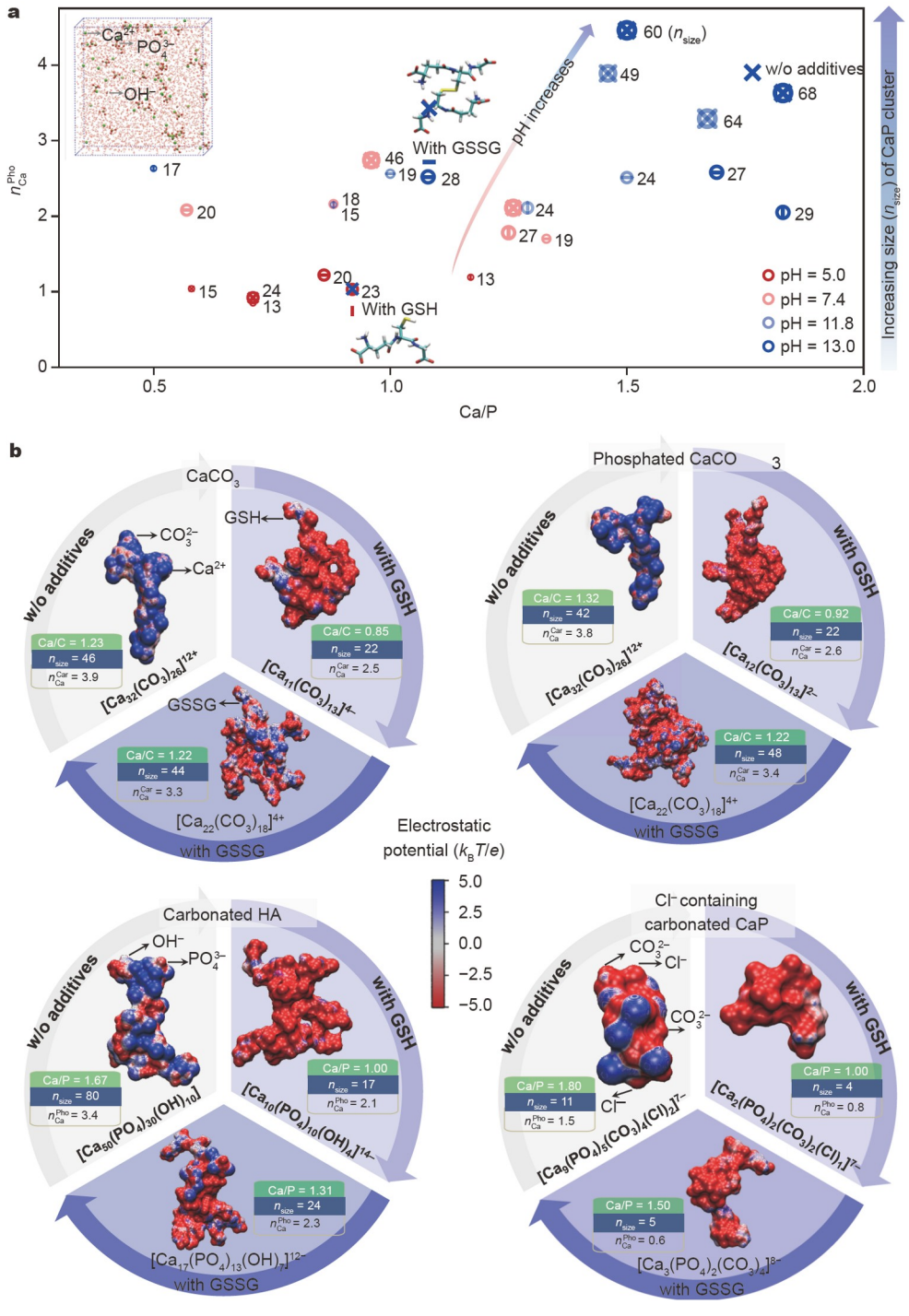

Figure 2 Formation of clusters denoted by Ca–O coordination number, cluster size, and electrostatic potential surface. (a) Change in the average Ca–O (from phosphate species) coordination number (n_{Ca}^{Pho}) and n_{size} as a function of Ca/P at 500 ns of MD simulation. The simulation model with the periodic boundary condition is illustrated in the inset. (b) The electrostatic potential surface maps and features of Ca/P (Ca/C), n_{size}, and n_{Ca}^{Car} (average Ca–O (from carbonate species) coordination number) (n_{Ca}^{Pho}) of $CaCO_3$, phosphated $CaCO_3$, carbonated HA, and Cl^- containing carbonated CaP (pH 13.0), respectively.

withCa/P = 2.00 (Table S20). As the simulation time increased, the CaP cluster size of CaP systems gradually increased (Fig. S21), because the number of free Ca^{2+} ions and phosphate species decreased. Although the total energy (*E*_Total) of the CaP systems fluctuated, the range of change was relatively small. The above results indicated that the nucleation of CaP was a dynamic process in solution, which is consistent with our previous experimental results [17]. When the CaP cluster size reaches a dynamic equilibrium, it starts crystallizing and nucleating to form CaP precipitates.

Interestingly, the Cl^-- and CO_3^{2-}-bearing CaP system had a large Ca/P of about 1.80 (Fig. 2b). The ΔG_b^{DFT} of Cl^- with Ca^{2+}

ion was −9.78 kcal mol^{-1}, which was greater than that between the Ca^{2+} ion and water (−1.64 kcal mol^{-1}). Thus, Cl^- ions were able to pass through the water layer and chelate with Ca^{2+} ions, thereby promoting the further coordination of Ca^{2+} ions with phosphate ions in SBF solutions and other chloride-bearing media.

Biological apatite identified from equilibrium oxygen isotope fractionation

To identify the exact forms of biological apatite in nature, the equilibrium oxygen isotope fractionation between phosphate and carbonate sites was estimated. The DFT calculated vibrational frequencies of carbonate and phosphate agree well with the available experimental data (Fig. S22), with a slope of 0.9999 ± 0.026 (1σ, R^2 = 0.9983). The calculated temperature dependences of equilibrium O isotope fractionation for carbonate (i.e., aragonite, calcite, and vaterite) and apatite-group minerals are shown in Fig. 3a and the polynomial fitting parameters of their RPFR as a function of temperature are reported in Table S21. The results show that carbonates with a $10^3\ln\beta$ of 91.44‰–92.97‰ at 298 K are more enriched in the heavy O isotope than phosphate with a $10^3\ln\beta$ of 84.74‰–80.99‰ at 298 K. The heavy O isotope is more enriched in calcite and vaterite than in aragonite, corresponding to a n_{Ca}^{Bulk} (coordination number of Ca^{2+} on bulk) of 9 in aragonite and 6 in calcite and vaterite. In the case of phosphate, the A-type HA ($Ca_{10}(PO_4)_6CO_3$, A-HA) is more enriched in the heavier O isotope than the B-type OH^--doped HA ($Ca_{10}(PO_4)_5(CO_3OH)(OH)_2$, B-HA-OH). The $10^3\ln\beta$ of these minerals decreased in the order of calcite = vaterite > aragonite > A-HA > FAp > ClAp > B-HA-Cl > B-type Na^+-doped HA ($NaCa_9(PO_4)_5(CO_3)(OH)_2$, B-HA-Na) > HA > B-HA-OH (Fig. 3a).

The O isotope fractionation between the carbonate site and phosphate site in apatite ($\Delta^{18}O_{carbonate\text{-}site\text{–}phosphate\text{-}site}$ = $10^3\ln\beta_{carbonate\text{-}site} - 10^3\ln\beta_{phosphate\text{-}site}$) decreases in sequence of A-HA > B-HA-Cl > B-HA-OH > B-HA-Na, and the $\Delta^{18}O_{carbonate\text{-}phosphate}$ values range from 1.54‰ to 5.44‰ at 298 K (Fig. S23). The different site-specific substitutions by CO_3 groups should lead to differences in the equilibrium O isotope fractionation, which could be distinguished by O isotope analysis using the secondary ion mass spectroscopy (SIMS) with an external analytical precision of ± 0.5‰.

The $10^3\ln\beta$ values of the individual CO_3 and PO_4 sites of minerals, correlate negatively with the average C–O and P–O bond lengths, respectively, showing that the strength of these bonds exercised the main control on the equilibrium O isotope fractionation (Fig. 3b). However, the CO_3 groups of aragonite and B-HA-Cl were twisted from planar to tetrahedral, causing them to deviate from the trend-line. For PO_4 groups, anionic Cl^- doping led to deviations in the $10^3\ln\beta$ value from the trend-line because of cell expansion. This was confirmed by Raman spectroscopic analyses (Fig. S24 and Table S22).

Carbonate defects in apatite lower the structural symmetry of the crystal compared with that of pure HA crystals, leading to the appearance of new IR-active vibrational modes (Fig. 3c) of ν_2 (CO_3) and $\nu_3(CO_3)$. By comparing the vibrational modes of CO_3^{2-} with experimental predictions, B-HA-Cl was fitted to the HA structure, for which both the characteristic vibration frequencies and the splitting peaks were within an acceptable error range (Table S23). The results of experiments involving HCO_3^- in this work (Fig. S25) and previous experimental studies [51–53] also support the location of those peaks for CO_3 and PO_4 groups. Bryant *et al.* [54] determined the O isotopic composition ($\delta^{18}O$) of CO_3 and PO_4 in horse enamel and bone, and obtained linear correlation between $\delta^{18}O_{carbonate\text{-}site}$ and $\delta^{18}O_{phosphate\text{-}site}$ (Fig. 3d). Based on the calculated isotherms for site-specific equilibrium isotopic fractionation of A-and B-ype HA minerals, only B-HA-Cl with an isotherm equation of $10^3\ln\alpha_{carbonate\text{-}site\text{–}phosphate\text{-}site} = 0.4413 \times 10^6/T^2 + 4.4298$ fitted the experimental data for the body temperature of mammals of 310 K. The above-mentioned results show that B-HA-Cl is the most likely type of biological apatite. This is also supported by the much lower E_{surf} of (001) surface for B-HA-Cl (0.36 J m^{-2}) compared with that of the HA (001) surface (1.08 J m^{-2}) (Fig. 1a). Based on the temperature-dependent oxygen isotope fractionation between the phosphate and hydroxyl sites of apatite as described by $10^3\ln\alpha_{phosphate\text{-}site\text{–}hydroxy\text{-}site} = 3.2825 \times 10^6/T^2 + 0.6929$, we proposed a geological thermometer that could be used to reconstruct paleo-temperatures using $\delta^{18}O$ in two specific O atom sites of HA (Section S3 of the Supplementary Information and Fig. S26).

The occurrence of apatite in materials as diverse as tooth enamel and mantle xenoliths is coupled with its capacity to incorporate fluorine and chlorine as essential structural constituents [55]. Pure end-members are uncommon in nature, but binary and ternary compositions are widely reported in igneous, metamorphic, and sedimentary rocks [56]. The concentrations of F^-, Cl^-, and OH^- are either correlated directly with physical properties such as etching rates and annealing characteristics [56] or are in a strong function of temperature, pressure, and composition [57], as fluorine and chlorine are important constituents of hydrothermal fluid in the Earth's crust and in mantle.

The role of this process was evaluated with MD simulations of the CaP system in an SBF solution. The MD simulations showed that the addition of Cl^- and HCO_3^- ions (as with an SBF solution) stabilized the carbonated CaP cluster through electrostatic attractions between the negatively charged ions (Cl^-, CO_3^{2-}, and HCO_3^-) and the exposed surface Ca^{2+} ions (Fig. 2b and Fig. S10). The MD snapshots of CaP clustering processes indicated that the Cl–Ca distance (2.85 Å) and O (carbonate)–Ca distance (2.35 Å) are close to those of the above-mentioned B-HA-Cl (Fig. 4 and Fig. S27), supporting the proposed B-HA-Cl model for biological apatite.

Reflections on apatite mineral deposition and different CaP phases

Subsequently, we designed the experiments by changing different factors, such as HCO_3^- concentrations ($[HCO_3^-]$), pH values, reaction temperatures, additives, and solvation environments (Section S4 of the Supplementary Information and Tables S24–S30) to investigate the effect of carbonate species and Cl^- ions on the CaP nucleation.

The early stage of CaP clustering and neucleation was simulated in a very dilute solution. The addition of GSH or GSSG additives did not induce obvious shifts in the amount of the formed CaP precipitation, as indicated by the UV-vis absorbance intensity measured in dilute solutions ($[Ca^{2+}] \approx 0.01$ mol L^{-1}) at pH ≈ 7.4 and 9.6 (Fig. S28). The above experimental results showed that the concentration of additives [17] was crucial to the formation of CaP precipitation in a very dilute solution.

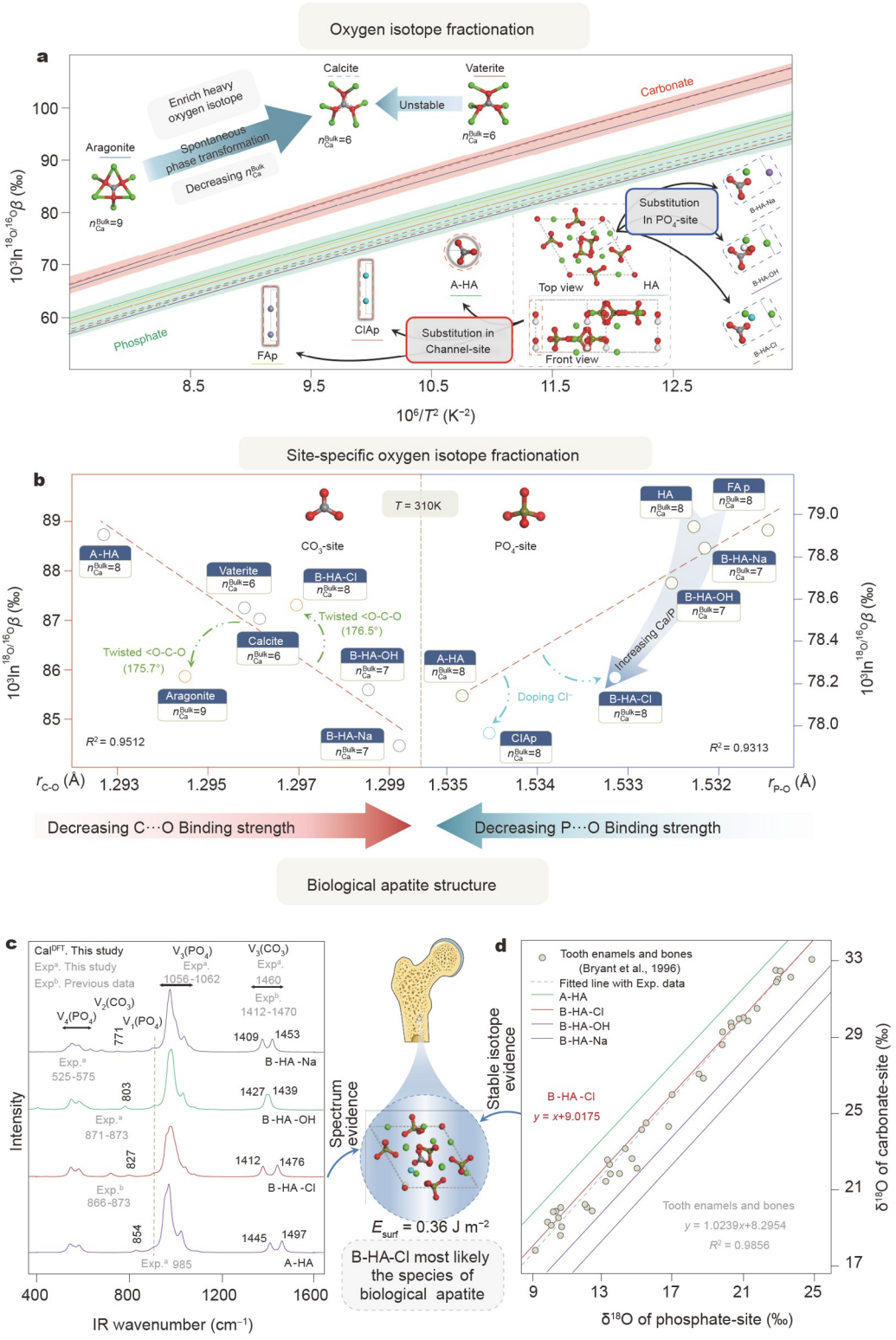

Figure 3 Equilibrium oxygen isotope fractionation analysis. (a) The RPFR ($10^3 \ln\beta$) of $^{18}O/^{16}O$ for carbonates and phosphates as a function of temperature. (b) The site-specific equilibrium O isotope fractionation of carbonate and phosphate in correlation with bonding length. (c) The IR spectra of A- and B-type apatite [51–53]. The black data represents the DFT calculated wavenumber with a scale factor of 1.0261 (Fig. S22). (d) The isotherms for the equilibrium fractionation between the carbonate site and phosphate site in A- and B-type apatites.

When the concentration of Ca^{2+} was increased to 0.2 mol L^{-1}, the initial pH value played a decisive role in regulating the composition of the CaP phase (Fig. 5a). The samples prepared at pH values about 5.0 and 9.6 were indexed to pure DCPD and HA phases by XRD and EDS analysis, respectively (Fig. 5a, b, Figs S29 and S30, and Table S31). The EDS analysis in Fig. S29c shows that the Ca/P ratios of all the samples prepared at pH ≈ 5.0 were in the generally accepted range of 0.8–0.9, consistent

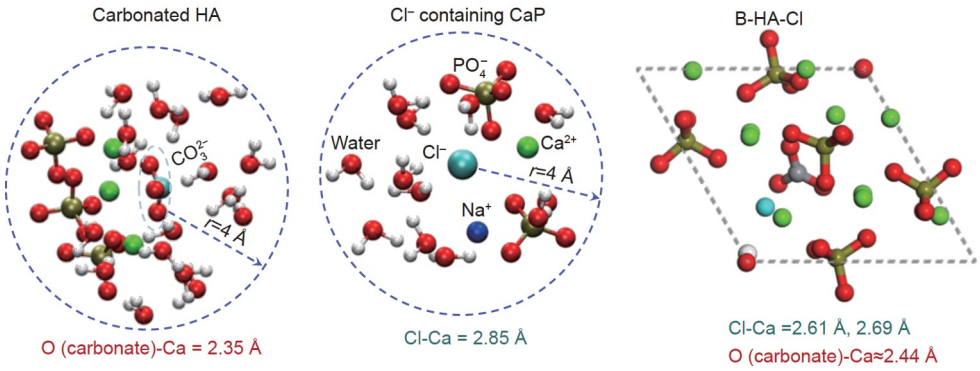

Figure 4 The selected MD snapshots from CaP (pH 13.0, SBF solution) and carbonated HA systems (the distance comes from the first peak in the radial distribution function, RDF), and unit cell of B-HA-Cl.

with the DCPD stoichiometry (Ca/P = 1.00). The CaP samples were DCPD in both the aqueous and SBF solutions at pH ≈ 7.4 and the reaction temperatures of RT and 310 K (Figs S31 and S32). When the reaction temperature increased to 343 K, the as-prepared sample was a mixture of DCPD and HA or pure HA (SBF solution) in the presence of GSH or GSSG additives (Fig. 5a). The above results suggest that a small increase in temperature and the addition of GSH or GSSG could promote HA crystallization from its precursor crystal DCPD in an SBF solution.

The important role of Cl^- ions in CaP nucleation in SBF solutions was demonstrated by the high concentration of Cl^- ions (0.125 mol L^{-1}) in the SBF solution (Table S3). The common occurrence of carbonate-substituted biological apatites [7,23] was also reflected from the experiments in the presence of CA (Microbe CA, C3640-5 mg > 2000 u, Fig. S33). The relative intensity of the (020) peak of DCPD decreased significantly as the [HCO_3^-] increased (Fig. S34), indicating that HA formation from DCPD precursor was favored by high [HCO_3^-]. The morphology of the crystals also changed, from sheet-like (DCPD) to granular (HA), as observed in the SEM images (Fig. 5c–h and Figs S29–S34).

In addition to anions, some cations, such as Mg^{2+} or Sr^{2+}, could affect the CaP morphologies, transforming from needle-like films to nanoflakes [58]. To test the effect of Mg^{2+} ions of SBF solution on the nucleation process of CaP, the contents of Ca and Mg in three prepared DCPD samples (pH ≈ 7.4, SBF solution) were detected by ICP-AES. The results showed that the three as-prepared DCPD samples did not contain detectable Mg element by ICP analysis (Table S32). Our DFT calculations in Table S33 indicate that the binding strength of Mg^{2+} ions with HPO_4^{2-} (ΔG_b^{DFT} = −18.77 kcal mol^{-1}) is much weaker than that of Ca^{2+} to the $CaHPO_4$ cluster (ΔG_b^{DFT} = −37.34 kcal mol^{-1}), implying little influence of Mg^{2+} ions. The above results suggest that the influence of Mg^{2+} ions on the nucleation process of CaP could be ignored. However, Sr^+ and Ca^{2+} have comparable binding free energies with HPO_4^{2-} ions (−39.33 kcal mol^{-1} *vs.* −37.34 kcal mol^{-1}). Usually, the concentration of Sr^{2+} ions is much lower than that of Ca^{2+} in biological systems, and thus the effect of competition between the trace Sr^{2+} and the abundant Ca^{2+} ions and phosphate species may be negligible.

Calcium and phosphorus are important inorganic components in biology, while silicon is also an important inorganic component in biological organisms (such as bone, teeth, collagen matrix, plants, phytoplankton, and zooplankton). Relevant studies have shown that Si-doped HA has significant changes in morphology and physiological proprieties, which promotes the activity of osteoblasts *via* the continuous release of Si, and is beneficial to the maintenance of bone integrity, collagen formation, and dentin mineralization [59]. The Si element involves in biological organisms *via* a variety of physicochemical processes, including the direct uptake of silicic acid by plant tissues [60], the formation of amorphous silica (e.g., phytoliths) [61], and the substitution into HA (e.g., bone) [62]. In comparison with Ca element, Si is present in trace amounts in biological organisms, the mechanisms of trace Si incorporation into organisms still remains unclear. The current study mainly focuses on the influence of major components in body fluids of biological organisms (i.e., carbonate species and chloride) on the nucleation process of biological apatite. The functional roles of trace elements (such as Cu, Mn, Si, and Li) in biogenic HA deserve to be investigated in the near future, including the competitive reactions during lattice substation and the critical effects of trace components on morphology, crystallinity, and solubility of HA. Moreover, silicate (SiO_3^{2-}) and carbonate (CO_3^{2-}) have comparable binding free energies with Ca^{2+} ions (−34.07 kcal mol^{-1} *vs.* −38.76 kcal mol^{-1}). This shows that silicate may compete with carbonate species to Ca^{2+} ions in the nucleation process of CaP.

It has been recognized that CA [63] can catalyze the interconversion of CO_2 and HCO_3^-. It has also been demonstrated that CA can promote the growth of $CaCO_3$ seeds in seawater [64]. Calcium is a vital element for living organisms that is mainly concentrated in bones (99%) and teeth [65]. In addition, human plasma contains more HCO_3^- (27 mmol L^{-1}), and Cl^- (103 mmol L^{-1}) ions than SO_4^{2-} ions (0.5 mmol L^{-1}) [66] (Table S3). When phosphate and carbonate species interact with Ca^{2+} ions in the body, CaP clusters doped with carbonate species and Cl^- ions form in the presence of additives in SBF solution, and crystallize into HA or Cl^--doped HA (B-HA-Cl). The above mentioned theoretical simulations and experimental observations could give a possible nucleation mechanism of biological apatite mineral deposition (Fig. 6).

CONCLUSION

The role of carbonate species and chloride ions in mediating inorganic phase nucleation of CaP has been revealed in this

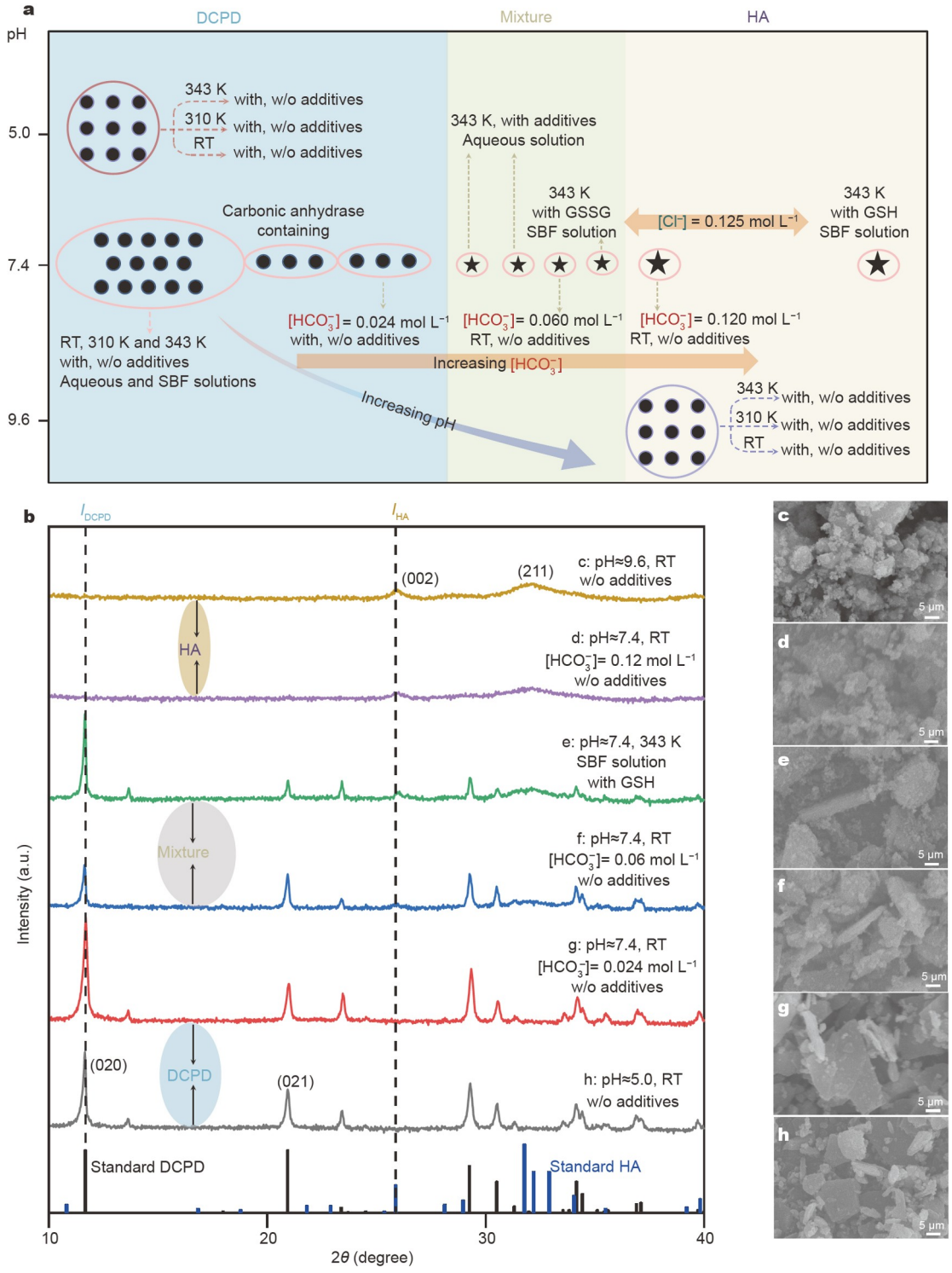

Figure 5 Formation of CaP phases as shown by XRD and SEM. (a) The distribution of DCPD and HA phases at different pH values. (b) XRD patterns of selected samples (DCPD, JCPDS#09-0077; HA, JCPDS#09-0432). (c–h) SEM images of selected samples with different experimental conditions. I_{DCPD} and I_{HA} are the intensities of the peaks at 2θ of 11.7° and 25.9°, respectively.

work by theoretical simulations, oxygen isotope fractionation, and experiments across multiple scales. The atomic-level MD simulations demonstrate that the addition of CO_3^{2-} ions decreases the aggregation of CaP through competitive interactions with free and active Ca^{2+} ions during the nucleation process of CaP. The stronger binding ability between Cl^- ions with Ca^{2+} ions than that between Ca^{2+} and water makes it possible for Cl^- ions to permeate the water shell and chelate with the exposed surface Ca^{2+} ions of the CaP cluster, thereby stabilizing the newly formed CaP phase. The equilibrium oxygen isotope fractionation between phosphate and carbonate sites of CO_3^{2-}-, Cl^--, and Na^+-doped HA was used to identify the possible forms of bio-

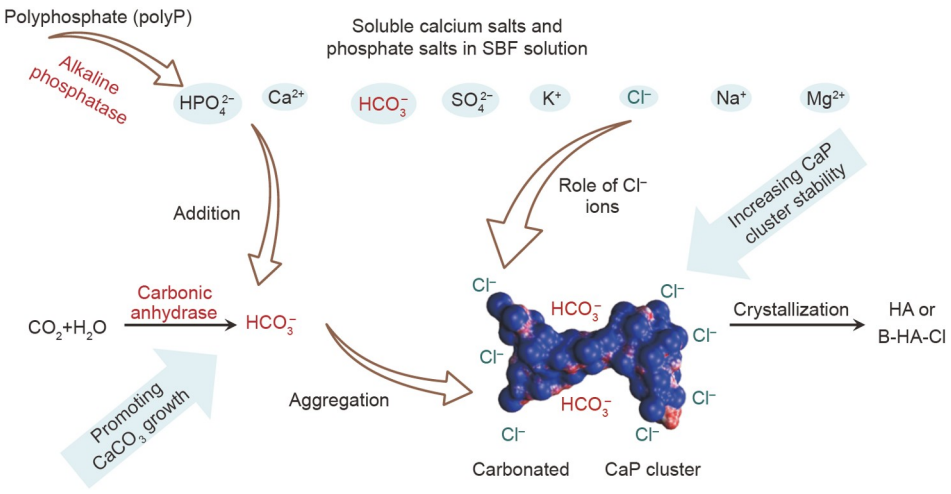

Figure 6 Biological apatite mineral deposition process.

logical apatite in nature. In combination with infrared and Raman spectroscopic analyses, the results of equilibrium oxygen isotope fractionation suggest that B-HA-Cl is the most likely type of biological apatite. DFT calculations reveal that B-HA-Cl (001) has a smaller E_{surf} than HA (001) surface, which further demonstrates that Cl^- ions can stabilize the CaP system.

In addition, a series of experiments with variable [HCO_3^-], pH values, reaction temperatures, additives, and solvation environments indicate that the initial pH value plays a decisive role in regulating the composition of the CaP phase. The formation of HA from the DCPD precursor is promoted by increasing [HCO_3^-]. When the reaction temperature increases from RT to 343 K, the as-prepared sample is HA instead of DCPD in the presence of additives and Cl^--bearing SBF solution.

The significant increase in understanding of biomineralization resulting from this study, including the important role of carbonate species, Cl^- ions and peptides identified using both theoretical and experimental approaches across different scales from electronic structures, atomic-level simulations, to morphologies, will help in the design of functional apatite materials and help constrain geological processes involving apatite. This would attract widespread attention from the multidisciplinary communities of chemistry, geology, biomaterials, environmental chemistry, and biology.

Received 25 October 2022; accepted 8 February 2023; published online 6 May 2023

1 Manoli F, Dalas E. Spontaneous precipitation of calcium carbonate in the presence of chondroitin sulfate. J Cryst Growth, 2000, 217: 416–421
2 Eliaz N, Metoki N. Calcium phosphate bioceramics: A review of their history, structure, properties, coating technologies and biomedical applications. Materials, 2017, 10: 334
3 Zhao H, Wu C, Gao D, *et al.* Antitumor effect by hydroxyapatite nanospheres: Activation of mitochondria-dependent apoptosis and negative regulation of phosphatidylinositol-3-kinase/protein kinase b pathway. ACS Nano, 2018, 12: 7838–7854
4 Zhang K, Zhou Y, Xiao C, *et al.* Application of hydroxyapatite nanoparticles in tumor-associated bone segmental defect. Sci Adv, 2019, 5: eaax6946
5 Tang Z, Li X, Tan Y, *et al.* The material and biological characteristics of osteoinductive calcium phosphate ceramics. Regen Biomater, 2018, 5: 43–59
6 Bayraktar D, Tas AC. Chemical preparation of carbonated calcium hydroxyapatite powders at 37°C in urea-containing synthetic body fluids. J Eur Ceramic Soc, 1999, 19: 2573–2579
7 Vallet-Regi M, González-Calbet JM. Calcium phosphates as substitution of bone tissues. Progr Solid State Chem. 2004, 32: 1–31
8 Müller W, Schröder H, Wang X. The understanding of the metazoan skeletal system, based on the initial discoveries with siliceous and calcareous sponges. Mar Drugs, 2017, 15: 172
9 Wu H, Li Z, Tang J, *et al.* The *in vitro* and *in vivo* anti-melanoma effects of hydroxyapatite nanoparticles: Influences of material factors. Int J Nanomed, 2019, Volume 14: 1177–1191
10 Singh S, Singh V, Aggarwal S, *et al.* Synthesis of brushite nanoparticles at different temperatures. Chem Papers, 2010, 64: 491–498
11 Furutaka K, Monma H, Okura T, *et al.* Characteristic reaction processes in the system brushite-naoh solution. J Eur Ceramic Soc, 2006, 26: 543–547
12 Štulajterová R, Medvecký Ľ. Effect of calcium ions on transformation brushite to hydroxyapatite in aqueous solutions. Colloids Surfs A, 2008, 316: 104–109
13 Jang HL, Lee HK, Jin K, *et al.* Phase transformation from hydroxyapatite to the secondary bone mineral, whitlockite. J Mater Chem B, 2015, 3: 1342–1349
14 Sun N, Jia Y, Wang C, *et al.* Dopamine-mediated biomineralization of calcium phosphate as a strategy to facilely synthesize functionalized hybrids. J Phys Chem Lett, 2021, 12: 10235–10241
15 Chen C, Qian J, Chen H, *et al.* Molecular origin of the biologically accelerated mineralization of hydroxyapatite on bacterial cellulose for more robust nanocomposites. Nano Lett, 2021, 21: 10292–10300
16 Hamai R, Toshima T, Tafu M, *et al.* Effect of anions on morphology control of brushite particles. Key Eng Mater, 2012, 529-530: 55–60
17 Chen H, Lv C, Guo L, *et al.* Surface stability and morphology of calcium phosphate tuned by pH values and lactic acid additives: Theoretical and experimental study. ACS Appl Mater Interfaces, 2022, 14: 4836–4851
18 Chu X, Jiang W, Zhang Z, *et al.* Unique roles of acidic amino acids in phase transformation of calcium phosphates. J Phys Chem B, 2011, 115: 1151–1157
19 Jiang W, Chu X, Wang B, *et al.* Biomimetically triggered inorganic crystal transformation by biomolecules: A new understanding of biomineralization. J Phys Chem B, 2009, 113: 10838–10844
20 Andersson SS, Wagner T, Jonsson E, *et al.* Apatite as a tracer of the source, chemistry and evolution of ore-forming fluids: The case of the Olserum-Djupedal REE-phosphate mineralisation, SE Sweden. Geochim Cosmochim Acta, 2019, 255: 163–187
21 Li Y, Li QL, Tang GQ, *et al.* Eppawala-AP, Sri Lanka, an apatite reference material for high precision chlorine isotope analysis. Atom Spectrosc, 2020, 41: 51–56
22 Li Y, Tang GQ, Liu Y, *et al.* Revisiting apatite SIMS oxygen isotope analysis and Qinghu-AP reference material. Chem Geol, 2021, 582:

120445
23 Vallet-Regi M, Navarrete DA. Biological apatites in bone and teeth. In: Vallet-Regi M, Navarrete DA (eds). Nanoceramics in Clinical Use: From Materials to Applications. 2nd ed. London: Royal Society of Chemistry, 2016. 1–29
24 Murugan R, Ramakrishna S. Development of nanocomposites for bone grafting. Compos Sci Tech, 2005, 65: 2385–2406
25 Hoang QQ, Sicheri F, Howard AJ, *et al.* Bone recognition mechanism of porcine osteocalcin from crystal structure. Nature, 2003, 425: 977–980
26 Piccoli PM, Candela PA. Apatite in igneous systems. Rev Mineral Geochem, 2002, 48: 255–292
27 Pan Y, Fleet ME. Compositions of the apatite-group minerals: Substitution mechanisms and controlling factors. Rev Mineral Geochem, 2002, 48: 13–49
28 Hughes JM, Rakovan JF. Structurally robust, chemically diverse: Apatite and apatite supergroup minerals. Elements, 2015, 11: 165–170
29 Konzett J, Frost DJ. The high P-T stability of hydroxyl-apatite in natural and simplified MORB—An experimental study to 15 GPa with implications for transport and storage of phosphorus and halogens in subduction zones. J Petrol, 2009, 50: 2043–2062
30 Murayama JK, Nakai S, Kato M, *et al.* A dense polymorph of $Ca_3(PO_4)_2$: A high pressure phase of apatite decomposition and its geochemical significance. Phys Earth Planet Inter, 1986, 44: 293–303
31 Chakhmouradian AR, Reguir EP, Zaitsev AN, *et al.* Apatite in carbonatitic rocks: Compositional variation, zoning, element partitioning and petrogenetic significance. Lithos, 2017, 274-275: 188–213
32 Ray JS, Shukla AD, Dewangan LK. Carbon and oxygen isotopic compositions of newania dolomite carbonatites, Rajasthan, India: Implications for source of carbonatites. Miner Petrol, 2010, 98: 269–282
33 Chiatti F, Corno M, Ugliengo P. Stability of the dipolar (001) surface of hydroxyapatite. J Phys Chem C, 2012, 116: 6108–6114
34 Frisch M, Trucks G, Schlegel H, *et al.* Gaussian 16. Wallingford CT: Gaussian Inc., 2016
35 Kresse G, Furthmüller J. Efficiency of *ab-initio* total energy calculations for metals and semiconductors using a plane-wave basis set. Comput Mater Sci, 1996, 6: 15–50
36 Kresse G, Furthmüller J. Efficient iterative schemes for *ab initio* total-energy calculations using a plane-wave basis set. Phys Rev B, 1996, 54: 11169–11186
37 Grimme S, Antony J, Ehrlich S, *et al.* A consistent and accurate *ab initio* parametrization of density functional dispersion correction (DFT-D) for the 94 elements H-Pu. J Chem Phys, 2010, 132: 154104
38 Pedregosa F, Varoquaux G, Gramfort A, *et al.* Scikit-learn: Machine learning in python. J Mach Learn Res, 2011, 12: 2825−2830
39 Case D, Cerutti D, Cheatham III T, *et al.* AMBER 2016. San Francisco: University of California, 2016
40 Wang J, Wolf RM, Caldwell JW, *et al.* Development and testing of a general amber force field. J Comput Chem, 2004, 25: 1157–1174
41 Baker NA, Sept D, Joseph S, *et al.* Electrostatics of nanosystems: Application to microtubules and the ribosome. Proc Natl Acad Sci USA, 2001, 98: 10037–10041
42 Bigeleisen J, Mayer MG. Calculation of equilibrium constants for isotopic exchange reactions. J Chem Phys, 1947, 15: 261–267
43 Urey HC. The thermodynamic properties of isotopic substances. J Chem Soc, 1947, 562
44 Li Y, Wang W, Huang S, *et al.* First-principles investigation of the concentration effect on equilibrium fractionation of K isotopes in feldspars. Geochim Cosmochim Acta, 2019, 245: 374–384
45 Clark SJ, Segall MD, Pickard CJ, *et al.* First principles methods using CASTEP. Z für Kristallogr, 2005, 220: 567–570
46 Wei ZY, Yang LJ, Gong SY, *et al.* Comparison of the microsolvation of CaX_2 (X = F, Cl, Br, I) in water: Size-selected anion photoelectron spectroscopy and theoretical calculations. J Phys Chem A, 2021, 125: 3288–3306
47 Krężel A, Bal W. Structure-function relationships in glutathione and its analogues. Org Biomol Chem, 2003, 1: 3885–3890
48 Zhang X, Wu FG, Liu P, *et al.* Enhanced fluorescence of gold nanoclusters composed of $HAuCl_4$ and histidine by glutathione: Glutathione detection and selective cancer cell imaging. Small, 2014, 10: 5170–5177
49 Naor MM, Nostrand KV, Dellago C. Car-Parrinello molecular dynamics simulation of the calcium ion in liquid water. Chem Phys Lett, 2003, 369: 159–164
50 Yang X, Wang M, Yang Y, *et al.* Physical origin underlying the pre-nucleation-cluster-mediated nonclassical nucleation pathways for calcium phosphate. Phys Chem Chem Phys, 2019, 21: 14530–14540
51 Trotter JA, Williams IS, Barnes CR, *et al.* Did cooling oceans trigger ordovician biodiversification? Evidence from conodont thermometry. Science, 2008, 321: 550–554
52 Lafon JP, Champion E, Bernache-Assollant D. Processing of AB-type carbonated hydroxyapatite $Ca_{10-x}(PO_4)_{6-x}(CO_3)_x(OH)_{2-x-2y}(CO_3)_y$ ceramics with controlled composition. J Eur Ceramic Soc, 2008, 28: 139–147
53 Yi H, Balan E, Gervais C, *et al.* A carbonate-fluoride defect model for carbonate-rich fluorapatite. Am Miner, 2013, 98: 1066–1069
54 Bryant JD, Koch PL, Froelich PN, *et al.* Oxygen isotope partitioning between phosphate and carbonate in mammalian apatite. Geochim Cosmochim Acta, 1996, 60: 5145–5148
55 Brenan J. Kinetics of fluorine, chlorine and hydroxyl exchange in fluorapatite. Chem Geol, 1993, 110: 195–210
56 Hughes JM, Cameron M, Crowley KD. Structural variations in natural F, OH, and Cl apatites. Am Miner, 1989, 74: 870–876
57 Zhu C, Sverjensky DA. Partitioning of F-Cl-OH between minerals and hydrothermal fluids. Geochim Cosmochim Acta, 1991, 55: 1837–1858
58 Lee K, Ko YM, Choe HC. Electrochemical deposition of hydroxyapatite substituted with magnesium and strontium on Ti-6Al-4V alloy. J Nanosci Nanotechnol, 2018, 18: 1449–1452
59 Saghiri MA, Vakhnovetsky J, Vakhnovetsky A. Functional role of inorganic trace elements in dentin apatite—Part II: Copper, manganese, silicon, and lithium. J Trace Elem Med Biol, 2022, 72: 126995
60 Wang W, Wei HZ, Jiang SY, *et al.* Adsorption behavior of metasilicate on *N*-methyl^{d}-glucamine functional groups and associated silicon isotope fractionation. Langmuir, 2016, 32: 8872–8881
61 Epstein E. The anomaly of silicon in plant biology. Proc Natl Acad Sci USA, 1994, 91: 11–17
62 Gibson IR, Best SM, Bonfield W. Chemical characterization of silicon-substituted hydroxyapatite. J Biomed Mater Res, 1999, 44: 422–428
63 Smith KS, Ferry JG. Prokaryotic carbonic anhydrases. FEMS Microbiol Rev, 2000, 24: 335–366
64 Wang YJ, Wei HZ, Jiang SY, *et al.* Mechanism of boron incorporation into calcites and associated isotope fractionation in a steady-state carbonate-seawater system. Appl Geochem, 2018, 98: 221–236
65 Theobald HE. Dietary calcium and health. Nutr Bull, 2005, 30: 237–277
66 Cüneyt Tas A. Synthesis of biomimetic Ca-hydroxyapatite powders at 37°C in synthetic body fluids. Biomaterials, 2000, 21: 1429–1438

Acknowledgements This work was supported by the National Natural Science Foundation of China (22033004 and 21873045). We are grateful to the High Performance Computing Centre of Nanjing University for providing the IBM Blade cluster system.

Author contributions Ma J and Chen H initiated the project. Chen H carried out the DFT calculations and MD simulations. Wei H, Wang J, and Willaims-Jones AE investigated the equilibrium O isotope fractionation among the minerals. Chen H, Guo L, Zheng L, Zhao C, and Xu W conceived the experiments and performed the characterizations (XRD, SEM, EDS, IR, and UV-Vis). Zhu Q performed the binding energy predication from ML. Zheng L calculated the surface energies of the apatite-like minerals. All authors contributed to the discussion of the results as well as the writing and revision of the manuscript.

Conflict of interest The authors declare that they have no conflict of interest.

Supplementary information Experimental details and supporting data are available in the online version of the paper.

Hongwei Chen is currently a PhD candidate at the School of Chemistry and Chemical Engineering, Nanjing University (NJU). His main research focuses on the nucleation of calcium phospahte.

Junlin Wang is currently a Master degree candidate at the School of Earth Sciences and Engineering, NJU. His research focuses on the first principles calculation of isotope geochemistry to understand the microscopic mechanism of isotope fractionation among minerals, fluids, and melts.

Haizhen Wei is a full professor in isotope geochemistry at the Department of Earth Sciences and Engineering, NJU. She received her PhD degree in geochemistry from the Graduate School of Chinese Academy of Sciences in 2006. Her research interests are in computation of stable isotope fractionation among minerals, melts and fluids based on density functional theory and *ab initio* molecular dynamics simulations and implication of stable isotope geochemistry for polymetallic ore deposits, paleoenvironmental changes and planetary evolution.

Lin Guo received her PhD degree in physical chemistry from NJU in 2000. She then worked at NJU as a lecturer from 2000 to 2003. At present, she is an associate professor at the Key Laboratory of Mesoscopic Chemistry of Ministry of Education and School of Chemistry and Chemical Engineering, NJU. Her research focuses on the design and synthesis of multifunctional nanomaterials for the application in biomedicine and environmental protection.

Jing Ma received her PhD degree in theoretical chemistry from NJU in 1998. She was a JSPS fellow (1998–2000) at Gifu University, Japan. After then she began to work at NJU as an associated professor (2000–2005) and professor of chemistry (since 2005). Her recent research is concentrated on the material datasets and machine learning models for data-driven material designs.

碳酸物种和氯离子对生物磷灰石磷酸钙成核的影响

陈红成[1†], 王俊霖[2†], A.E. Willaims-Jones[3], 朱琴[1], 郑利锋[1], 赵晨晨[1], 刘子腾[1], 徐伟高[1], 魏海珍[2*], 郭琳[1*], 马晶[1*]

摘要 磷灰石是骨骼和牙齿等生物硬组织的主要无机成分，对脊椎动物至关重要. 生物系统的体液中普遍存在碳酸物种和Cl^-离子，了解这些阴离子对生物磷灰石成核过程的影响有助于解释生物矿化的控制作用. 理论研究表明，Ca–O配位数在CaP成核和CaP与添加剂的界面相互作用中是一个重要描述符. CaP团簇最外层的Ca^{2+}离子能够通过静电作用吸引碳酸物种和Cl^-离子，从而促进CaP相的形成. 在碳酸物种和Cl^-离子存在的情况下，钙磷石(DCPD)可以转化为羟基磷灰石(HA). 平衡氧同位素分馏和振动光谱分析结果表明，Cl^-离子掺杂的B型HA是最有可能的生物磷灰石. 上述结果可以指导阴离子掺杂的具有生物功能的磷灰石材料的合成.

